

This work is on a Creative Commons Attribution 4.0 International (CC BY 4.0) license, <https://creativecommons.org/licenses/by/4.0/>. Access to this work was provided by the University of Maryland, Baltimore County (UMBC) ScholarWorks@UMBC digital repository on the Maryland Shared Open Access (MD-SOAR) platform.

Please provide feedback

Please support the ScholarWorks@UMBC repository by emailing scholarworks-group@umbc.edu and telling us what having access to this work means to you and why it's important to you. Thank you.



Aluminum-alloyed lightweight stainless steels strengthened by B2-(Ni, Fe)Al precipitates

M. Harwarth^a, G. Chen^{a,b}, R. Rahimi^c, H. Biermann^d, A. Zargaran^e, M. Duffy^f, M. Zupan^f, J. Mola^{a,*}

^a Materials Design and Structural Integrity Laboratory, Faculty of Engineering and Computer Sciences, Osnabrück University of Applied Sciences, 49076 Osnabrück, Germany

^b The State Key Laboratory of Refractories and Metallurgy, Wuhan University of Science and Technology, 430081 Wuhan, China

^c Formerly with Institute of Iron and Steel Technology, Technische Universität Bergakademie Freiberg, 09599 Freiberg, Germany

^d Institute of Materials Engineering, Technische Universität Bergakademie Freiberg, 09599 Freiberg, Germany

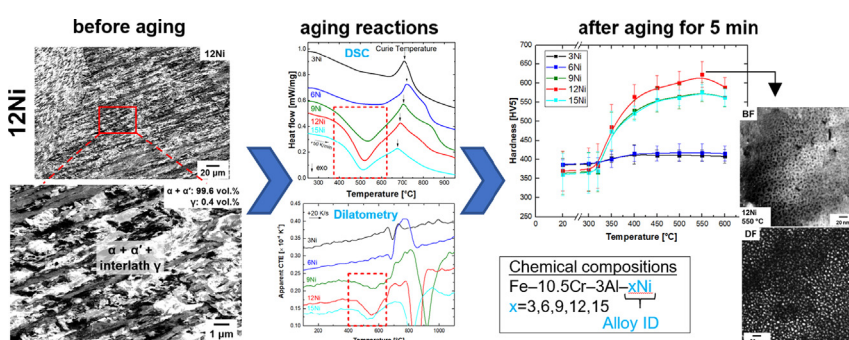
^e Graduate Institute of Ferrous Technology (GIFT), Pohang University of Science and Technology (POSTECH), Pohang 37673, Republic of Korea

^f Department of Mechanical Engineering, University of Maryland, Baltimore County, 1000 Hilltop Circle, Baltimore, MD 21250, USA

HIGHLIGHTS

- Ni addition enables microstructures from fully ferritic to martensitic-austenitic.
- Solute Al and Ni in martensite cause a pronounced age-hardening response.
- Age hardening arises from the formation of B2-(Ni,Fe)Al precipitates.
- Peak hardness is similar to maraging grade 300 and superior to PH stainless steels.
- B2 Formation in martensite is associated with heat release and a net contraction.

GRAPHICAL ABSTRACT



ARTICLE INFO

Article history:

Received 20 November 2020

Revised 21 April 2021

Accepted 7 May 2021

Available online 08 May 2021

Keywords:

Lightweight steel

Al addition

Stainless steel

Martensite

B2-(Ni,Fe)Al

Intermetallic precipitates

ABSTRACT

The age hardenability of Al-alloyed lightweight stainless steels with the base chemical composition Fe-10.5Cr-3Al (wt.%) and Ni concentrations in the range 3–15 wt.% was studied. Alloys containing 3% and 6% Ni exhibited almost fully ferritic matrix microstructures and a weak age hardening response. Alloys containing 9%, 12%, and 15% Ni, on the other hand, developed primarily martensitic microstructures. Differential scanning calorimetry measurements indicated the occurrence of an exothermic reaction in the approximate temperature range 375–625 °C. Dilatometry measurements indicated that the exothermic reaction was accompanied by a net contraction. Hardness measurements after aging for 5 min indicated significant hardening of alloys already at 350 °C due to the formation of B2-(Ni,Fe)Al intermetallic precipitates. The age hardening response was significantly superior to that of conventional precipitation-hardenable martensitic stainless steels. Tensile elongation in the aged condition was negatively influenced by the presence of soft ferrite regions. Processing conditions associated with a fully martensitic microstructure prior to aging are required to render a uniform age hardening response. Guidelines for the development of a new family of lightweight precipitation-hardenable steels with lower raw material costs and a higher corrosion resistance compared to the standard 18Ni maraging steels are provided.

© 2021 The Author(s). Published by Elsevier Ltd. This is an open access article under the CC BY license (<http://creativecommons.org/licenses/by/4.0/>).

* Corresponding author.

E-mail addresses: michael.harwarth@hs-osnabrueck.de (M. Harwarth), g.chen@hs-osnabrueck.de (G. Chen), biermann@ww.tu-freiberg.de (H. Biermann), alireza@postech.ac.kr (A. Zargaran), mduffy1@umbc.edu (M. Duffy), mzupan@umbc.edu (M. Zupan), j.mola@hs-osnabrueck.de (J. Mola).

1. Introduction

Due to its high strength and low cost, steel is the material of choice for a variety of engineering applications [1]. The addition of light elements such as Al to steels is one of the measures to reduce the density of steels and make them attractive for lightweight design, where the specific strength is of the highest priority [2–4]. The inherently low corrosion resistance can be enhanced by the addition of Cr, leading to the group of stainless steels for applications involving aggressive media or to increase the service life under atmospheric conditions [5]. The strength and ductility of stainless steels can be adjusted by the design of the microstructural constituents [5]. The latter design is aided by thermodynamic calculations or empirical approaches which take the effect of alloying elements on the microstructure development into consideration [6]. The empirical approaches are best exemplified by the common use of the Schaeffler diagrams to take into account the influence of alloying elements on the phases present at room temperature (RT) [6–9].

Apart from the clear effect of the matrix microstructure type on the achieved properties, the strength of stainless steels can be raised by additional strengthening mechanisms such as solid solution hardening and precipitation hardening. In austenitic stainless steels, the high solubility of interstitial alloying elements enables the addition of large quantities of alloying elements such as C and N for the purpose of solid solution hardening [10–13]. In martensitic and ferritic stainless steels, on the other hand, precipitation hardening becomes the mechanism of choice [14–16]. If the matrix and precipitates remain stable up to high temperatures, a high creep resistance at elevated temperatures may also be achieved [17]. Researches on Fe–Al–Ni alloys have indicated a ready formation of intermetallic compounds [18]. This offers the potential to harden ferritic steels by for instance B2-ordered NiAl precipitates [19–21]. Analogous to Ni-based superalloys with a disordered face-centered cubic matrix (γ) in which the occurrence of ordered coherent Ni_3Al (γ') precipitates – with a lattice parameter similar to the matrix – causes substantial strengthening, the formation of ordered B2 precipitates in ferritic steels can be used to strengthen Al-added ferritic and martensitic alloys. In such cases, lattice strains induced by coherency (lattice parameters of B2 and ferrite being 2.887 Å and 2.866 Å, respectively [22,23]) can contribute to a higher strength [24]. By the formation of a large volume fraction of B2 precipitates, steels containing Ni and Al can exhibit an excellent creep resistance at elevated temperatures [17,25,26].

Povoden-Kardeniz et al. [27] simulated the course of precipitation reactions upon aging of a PH 13–8 Mo martensitic stainless steel. Initially, precipitates of type $\text{Fe}_{0.63}\text{Ni}_{0.21}\text{Al}_{0.11}\text{Cr}_{0.047}\text{Mo}_{0.006}$ were predicted to form within seconds of exposure to 575 °C. After a longer heat treatment time, the precipitates composition approached towards NiAl.

The formation of B2-(Ni,Fe)Al precipitates in Fe–10Cr–10Ni–3.4Mo–(3–10)Al (wt.%) ferritic steels and its influence on the mechanical properties have been examined in recent investigations [28,29]. In ferrite-containing high Mn steels, ordered B2 precipitates only appear as domains in the disordered ferrite, therefore complicating the identification of precipitates without diffraction analysis in transmission electron microscope (TEM) [30,31].

In the present work, the formation of B2-(Ni,Fe)Al precipitates in C-free Fe–Cr–Al–Ni steels with various Ni contents was studied by scanning electron microscopy (SEM), TEM, differential scanning calorimetry (DSC) and dilatometry. The latter two techniques enable to analyze solid-state phase transformations during continuous heating or cooling treatments. The varied Ni content resulted in the development of different matrix microstructures—from fer-

ritic to martensitic to austenitic-martensitic with increasing Ni content—thereby enabling to evaluate the effect of the matrix type on B2 precipitation. Due to the high Cr content of 10.5 wt.% in the alloys, the results presented are relevant to the design of B2-strengthened stainless steels. Furthermore, they contribute to the enhancement of thermodynamic databases, especially with regard to the transformation temperatures, matrix type, and the possibility of precipitates formation.

2. Materials and methods

Fe–Cr–Al–Ni alloys with different Ni amounts were produced in a cold-crucible induction melting facility. Ingots were semi-spherical in shape and weighed approximately 300 g. The chemical compositions are shown in Table 1. The design of the chemical compositions was based on our prior experiences with a ferritic Fe–17Cr–9Ni–7Al–6Mn–0.46C (wt.%) stainless steel capable of B2 formation [31]. The microstructure of the latter alloy contained a large fraction of Cr-rich carbides. These carbides are excluded in present alloys by eliminating C from the chemical composition. Furthermore, since the investigation of B2 precipitates in martensite is central to the present work, the chemical compositions were adjusted while aiming for martensite at RT. This necessitated a relatively high austenite potential to ensure its formation at the solution annealing temperature and a relatively low content of alloying elements to ensure high martensite start (M_s) temperatures and martensitic transformation during cooling to RT.

The cast ingots were homogenized at 1200 °C for 3 h. The blow of N_2 gas yielded an average cooling rate of 2.5 K/s in the temperature range 1200–600 °C. N_2 flow rate was maintained constant at lower temperatures. Due to the reduced temperature difference between ingots and the blown N_2 gas, the heat transfer rate continuously decreased at lower temperatures. Accordingly, cooling rate continued to decrease below 600 °C. Specimens for DSC and dilatometry experiments were used in the as-homogenized condition. Microstructures in the as-homogenized condition were examined by SEM (Zeiss Ultra 55 field-emission SEM). Aging heat treatment of specimens in the as-homogenized condition was done using $5 \times 5 \times 5 \text{ mm}^3$ cuboid specimens and consisted of an isothermal treatment for 5 min in a muffle furnace followed by quenching in water. Microstructural examinations in the aged condition were done using a Zeiss Auriga field-emission SEM or a Zeiss Libra 120 TEM with a LaB_6 -type gun operated at 120 kV. For higher spatial resolutions, a JEOL JEM-2100F type TEM operated at an accelerating voltage of 200 kV was used. The JEOL TEM was equipped with double spherical aberration correctors for energy-dispersive X-ray spectroscopy (EDS). Specimens for TEM examinations using the JEOL microscope were resolution heat treated prior to aging. The intermediate solution treatment was also applied to the specimens for the tensile tests. DSC measurements were done in a DSC 404C Pegasus thermal analyzer. For the measurements, specimens with dimensions of $5 \times 5 \times 5 \text{ mm}^3$ were placed in Al_2O_3 crucibles. Heating and soaking steps were done in vacuum. DSC heating and cooling rates were 50 K/min and 10 K/min, respectively. To examine

Table 1
Nominal chemical composition of alloys in wt.%.

Alloy ID	Ni	Al	Cr	Fe
3Ni	3	3	10.5	balance
6Ni	6	3	10.5	balance
9Ni	9	3	10.5	balance
12Ni	12	3	10.5	balance
15Ni	15	3	10.5	balance

the reproducibility of the experiments and identify possible artifacts, DSC measurements were performed using two specimens from each condition.

Dilatometry measurements in a BÄHR-DIL805 dilatometer were done using specimens $3.5 \times 3.5 \times 10 \text{ mm}^3$ in size. Initially, as-homogenized specimens were heated to 1200°C in vacuum. After a soaking time of 1 min, specimens were cooled to RT by blowing Ar into the chamber. For each specimen, this thermal treatment was performed twice. Heating and cooling rates in dilatometry cycles were 20 K/s and 50 K/s, respectively.

Specimen preparation for SEM examinations consisted of mechanical grinding and polishing. The final polishing step was done in a vibration-polisher for 24 h. Non-crystallizing colloidal silica suspension was used as the polishing agent. TEM specimens were prepared by mechanical grinding to a thickness of approximately $100 \mu\text{m}$ followed by twin-jet polishing at 0°C with an electrolyte of 5 pct perchloric acid in 95 pct acetic acid.

X-ray diffraction (XRD) measurements were done in a BRUKER D8 Advance diffractometer with a Cu anode ($\lambda = 1.54060 \text{ \AA}$) in Bragg-Brentano geometry.

Vickers hardness tests were done with a WOLPERT universal hardness tester in accordance with the DIN EN ISO 6507-1 standard [32]. Due to the limited material availability, tensile tests were done using microtensile specimens. The materials were cut into individual microtensile specimens using a Fanuc Alpha OiE wire electric discharge machine (EDM). The EDM cutting parameters have been optimized to minimize effects on the as-samples; specifically, the cut layer associated with EDM processing has been evaluated and proven not to modify mechanical testing results [33–35]. The as-machined microtensile specimens have a nominal footprint of $3 \text{ mm} \times 1 \text{ mm}$, and tensile gauge section of $\sim 0.250 \text{ mm}^2$. After machining, the specimen surfaces were prepared using traditional metallographic methods by polishing with 180, 320, 400, 600, 800 and 1200 grit SiC papers and water flush for cleaning and lubrication. The SiC polishing preparation is followed by a $0.05 \mu\text{m}$ colloidal silica suspension polish. Specimen preparation is finished with a vibratory polish using a 9:1 ratio of $0.05 \mu\text{m}$ colloidal silica and 30% hydrogen peroxide. This final polish is a hybrid mechanical and chemical polish which results in a mirror finish of the specimen surfaces. The microtensile specimens were tested using a purpose-built microtesting system located at UMBC—University of Maryland, Baltimore County. The load frame uses a piezoelectric actuator, using a load cell with a resolution of 0.0022 N. A linear air bearing is implemented as a loading frame to remove any friction during the test and ensure uniaxial loading. The system utilizes digital image correlation (DIC) for non-contact strain measurements directly within the gauge section. Additional information concerning the test system has been previously reported [33,35,36]. In this study all specimens were tested at a quasi-static strain rate of 10^{-4} s^{-1} , at RT, with monotonic loading until failure. Samples of this size prepared as described have a proven effect on measuring the mechanical properties of a variety of materials [33–35,37,38].

The ferromagnetic phase fraction (ferrite + martensite) of specimens with various Ni contents in the as-homogenized condition was determined by magnetic measurements. Magnetic measurements were done using a Metis MSAT device equipped with a Lakeshore 480 fluxmeter (magnetic field intensity $> 3.77 \text{ kOe}$). The equipment returns the ferromagnetic phase content after accounting for the effect of alloying elements through an internal calibration. Further calibration of the chemical composition effect, especially the effect of Ni on the mass magnetization, was done by measuring the mass magnetization of reference specimens with known ferromagnetic phase fractions and chemical compositions resembling those of the alloys used in the present work.

3. Results and discussion

3.1. Microstructures before aging

The microstructures of alloys in the as-homogenized condition were studied by electron channeling contrast imaging (ECCI) in SEM. Fig. 1 shows the microstructure for the 3Ni and 6Ni alloys. Whereas the microstructure of the 3Ni alloy consists entirely of ferrite (Fig. 1(a)), the 6Ni alloy additionally exhibits a phase contrast due to the martensite in the vicinity of some grain boundaries (Fig. 1(b)). Accordingly, ferromagnetic measurements confirmed that both steels consisted entirely of ferromagnetic phases.

According to the inset in Fig. 1(b), the 6Ni alloy is capable of developing a small fraction of austenite at high temperatures. This grain boundary austenite with a Widmanstätten morphology transforms to martensite during subsequent cooling to RT. Due to the predominantly ferritic microstructure at all temperatures, the dilatometry curves of 3Ni and 6Ni alloys during cooling from 1200°C did not exhibit any remarkable length changes due to phase transformations (Fig. 2). The only indication for the occurrence of some martensitic transformation in the 6Ni alloy was the reduced dilatometry slope (decrease in the apparent coefficient of thermal expansion, CTE_a) at low temperatures. Accordingly, the vertical distance between the dilatometry curves for 3Ni and 6Ni alloys decreased at temperatures below approximately 500°C .

Optical and SEM micrographs of 9Ni, 12Ni, and 15Ni alloys are shown in Fig. 3. The optical micrographs in the left-hand column of Fig. 3 have been etched using Beraha solution to highlight ferrite with a dark contrast. Based on the optical micrographs, ferrite is present in the as-homogenized microstructure of all alloys but to a larger extent in the 9Ni alloy. According to the SEM micrographs in the second and third columns of Fig. 3, the microstructure of all alloys predominantly consists of areas with a contrast similar to that of martensite in the 6Ni alloy (Fig. 1(b)). Ferromagnetic phase fractions of alloys are also marked in Fig. 3 and support that the contrast changes in SEM micrographs are mainly due to the presence of martensite. Since the 9Ni alloy was found to be entirely ferromagnetic, the lamellae with a relatively dark contrast in the SEM micrographs (Fig. 3(b,c)) are expected to be ferrite. Ferrite is expected to have formed during cooling from the homogenization temperature. This interpretation is consistent with the observation of a small endothermic peak during DSC cooling of 9Ni alloy from the liquid range at a rate of 10 K/min (not shown). The spatial distribution of ferrite lamellae in the optical micrograph of Fig. 3(a) implies the existence of chemical composition inhomogeneities originating from the solidification segregation [39]. EDS linescan across one of the lamellae (Fig. 4(a,c)) confirms that it is enriched with Al and Cr and depleted of Ni. Given the high ferrite potential of the 9Ni alloy and its ferritic solidification mode as confirmed by the DSC measurements presented later, the lamellae correspond to the dendrite cores. Dendrites are enriched with Al and depleted of Cr and Ni during ferritic solidification [40,41]. The high Al content of such regions in turn favors their transformation of ferrite and the co-partitioning of Cr during subsequent processing steps. Fine-scale chemical composition inhomogeneities created by prior processing steps are the basis for novel heat treatment routes such as the chemical patterning of medium Mn steels [42]. By means of dilatometry, M_s temperature for the 9Ni alloy was found to be approximately 292°C (Fig. 2), indicating that the martensitic transformation can proceed until completion, as also confirmed by magnetic measurements.

In the 12Ni alloy with a higher austenite potential than the 9Ni alloy, a smaller fraction of lamellar ferritic regions is implied by the optical micrographs (Fig. 3(d)). Given that the M_s temperature is nearly 156°C for the 12Ni alloy, regions with a bright contrast in

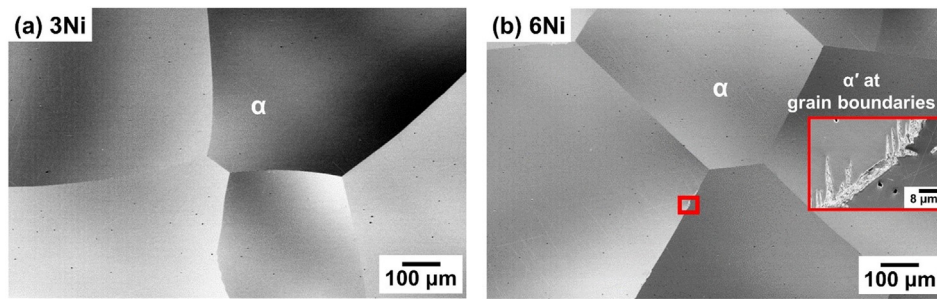


Fig. 1. SEM micrographs of as-homogenized specimens of (a) 3Ni and (b) 6Ni alloys. Both specimens consist of large ferrite grains. The inset in (b) shows small amounts of martensite at grain boundaries.

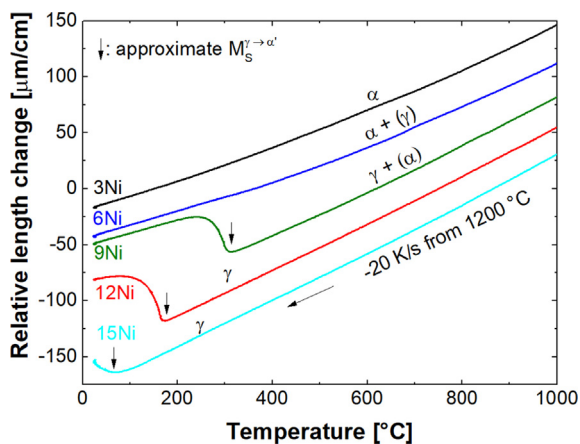


Fig. 2. Changes in the length of dilatometry specimens quenched from 1200 °C to RT. In contrast to 3Ni and 6Ni alloys, 9Ni, 12Ni, and 15Ni alloys exhibit remarkable expansions due to martensite formation. The onset of expansions (M_s temperatures) are marked by vertical arrows. For clarity, curves were translated vertically.

the optical micrograph are primarily martensite. Phase contrast between the small fraction of ferrite and martensite in the SEM micrographs (Fig. 3(e,f)) is not high enough to enable a ready distinction. Similar to the 9Ni alloy, the small fraction of ferrite in the 12Ni alloy is expected to have been triggered due to a prior segregation of alloying elements (Fig. 4(b,d)). In addition to ferrite and martensite, the microstructure of the 12Ni alloy consists of a negligible amount of interlath austenite, as implied from the ferromagnetic phase fractions.

In the 15Ni alloy with the highest Ni content and lowest M_s temperature of all alloys (about 50 °C), the ferromagnetic phase content decreased to 72.2 vol.% suggesting the coexistence of a considerable fraction of austenite with martensite. Referring to the optical micrograph of Fig. 3(g), regions with a bright contrast are austenite. In spite of the low ferrite potential of the 15Ni alloy, ferritic regions with a dark contrast were also observed in the optical micrograph of the 15Ni alloy. Based on the DSC results discussed later, the 15Ni alloy exhibits an austenitic solidification mode. Due to the inverse segregation of Ni (i.e. enrichment in austenite dendrites during solidification) [43] and the rejection of Al and Cr to the liquid [40,44], the spatial distribution of austenite and ferrite in the 15Ni alloy is expected to correspond to that of dendrite cores and interdendritic regions, respectively. In the SEM micrographs of Fig. 3(h,i), austenitic regions are primarily those with a uniform contrast, as marked in Fig. 3(i). Nevertheless, the presence of finer interlath austenite regions cannot be excluded. Furthermore, the low mechanical stability of austenite in steels with M_s temperatures near or above RT [11] implies that

some of the austenite might have transformed to martensite during specimen preparation for microstructural examinations.

Based on the difference in the M_s temperature of 9Ni, 12Ni, and 15Ni alloys, the addition of each wt.% Ni to the present alloy system decreases the M_s temperature by about 41 K (Fig. 5). This is larger than the coefficients suggested for Ni in the empirical relationships to predict M_s temperature in low-alloy steels [45–47]. This deviation indicates the noticeable effect of the base chemical composition and is likely aided by the coexistence of Ni and Al in the present alloy system.

To study the microstructure evolution of alloys during solidification and at temperatures relevant to the solution heat treatment, DSC measurements were performed at temperatures up to 1550 °C, the results of which are summarized in Fig. 6. Instead of using the DSC signal collected during cooling from 1550 °C for the interpretation of the sequence of reactions during solidification, the DSC signal during heating was used. This was intended to avoid the following three problems. The first problem associated with the use of the data collected during cooling from the liquid range is the change in the morphology of specimens from cuboidal to spherical due to the surface tension effects. This effect reduces the contact area of specimens with the crucible, thereby weakening the DSC signal. The second problem is the higher risk of changes in the chemical composition of alloys due to the reaction of molten alloys with impurities that might still be present in the evacuated DSC chamber. Finally, the possibility of applying a higher heating rate (compared to the maximum applicable cooling rate) and an increased heat exchange per unit time enhances the sensitivity of the acquired data [48].

As marked in Fig. 6, the solidification of 3Ni, 6Ni, 9Ni, and 12Ni alloys begins with the formation of ferrite. For the 3Ni alloy, ferrite persists from RT up to the liquid range. For the 6Ni alloy with a small fraction of grain boundary austenite at high temperatures, the peak due to the transformation of austenite (product of the reversion of martensite) to ferrite could not be accurately identified in the shown temperature range. In contrast, the endothermic peaks due to the formation of ferrite from austenite in the 9Ni and 12Ni alloys could be readily identified and are marked by arrows in the inset of Fig. 6. During the reverse process of cooling from the liquid range, the ferrite formed during solidification will transform to austenite over temperature ranges corresponding to these peaks. For the 12Ni alloy, the formation of austenite from ferrite begins shortly below the solidus temperature. For the 15Ni alloy with the highest austenite potential of all alloys, no intermediate peak due to the formation of ferrite was detected. This indicates that the solidification mode has changed from ferritic to austenitic.

The transformation temperature ranges inferred from the DSC results are summarized in Fig. 7(a). Since the transformation temperatures were determined based on the results during continuous heating, they might somewhat overestimate equilibrium transfor-

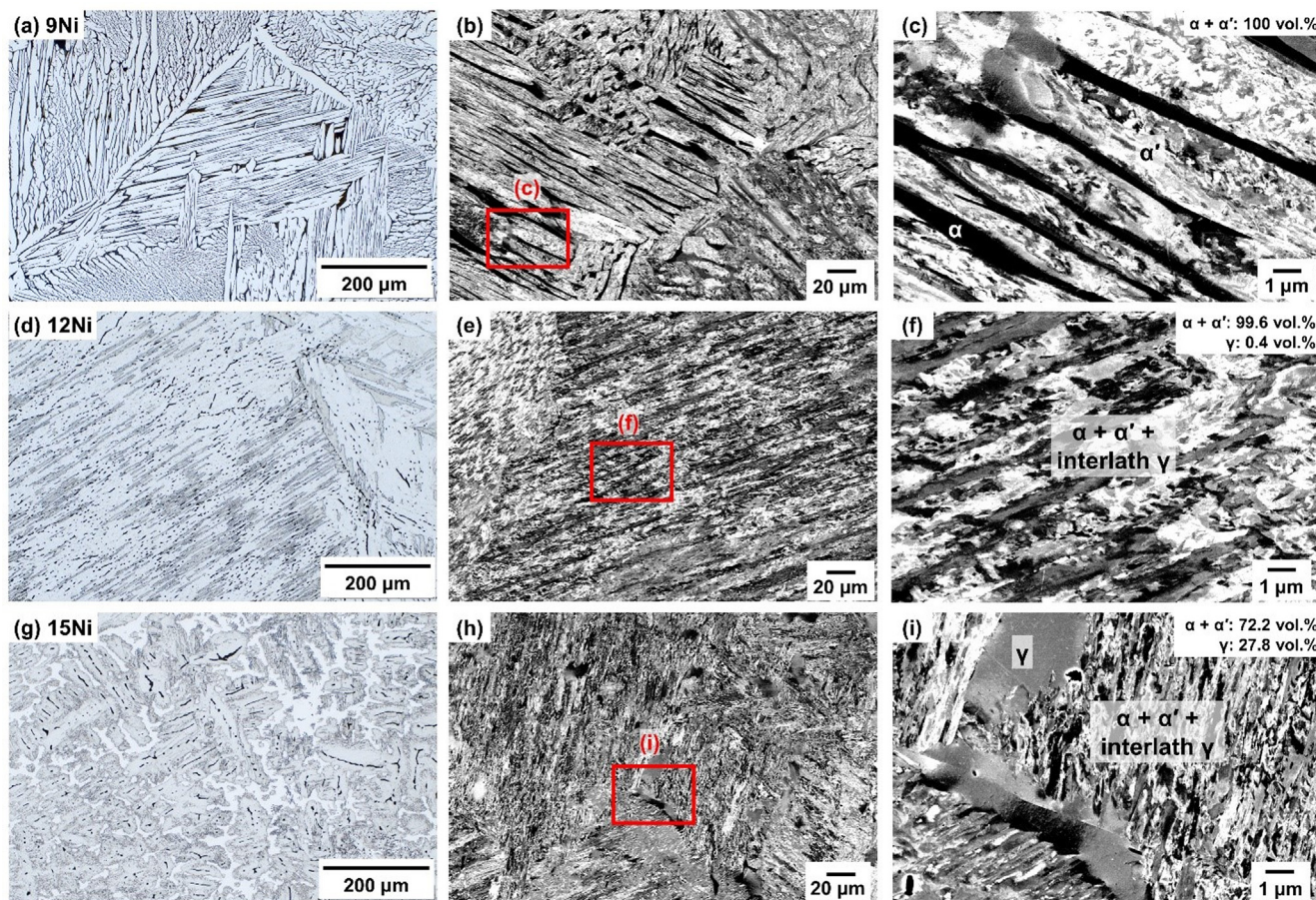


Fig. 3. Light optical micrographs (left column) and SEM micrographs (middle and right columns) of as-homogenized specimens of (a-c) 9Ni, (d-f) 12Ni, and (g-i) 15Ni alloys.

mation temperatures. Such an overestimation is expected based on the kinetics of diffusional phase transformations [49,50]. For comparison, the pseudo-binary Fe-10.5Cr-3Al-(0-20)Ni (wt.%) phase diagram calculated by the TCFE9 database of Thermo-Calc is shown in Fig. 7(b). An enlarged view of the section marked by a dashed rectangle is provided in Fig. 7(c). In terms of the solidification mode and the sequence of transformations at high temperatures, the calculated results show a good agreement with the DSC results. However, the liquidus temperature curve in the calculated results is somewhat lower than the DSC results. For the 3Ni alloy, for instance, the calculated liquidus temperature is 1520 °C whereas the DSC-based liquidus temperature is nearly 1550 °C. The calculated solidus temperatures show a better agreement with the DSC results. In other words, the mushy zone in the thermodynamic calculations is narrower than determined from the experimental DSC results.

3.2. Aging treatment

3.2.1. Thermal analysis of aging reactions by DSC and dilatometry

To study the microstructural changes during reheating of as-homogenized specimens, the low temperature region of the DSC traces obtained during continuous heating were analyzed. All alloys exhibited an endothermic peak in the vicinity of 700 °C (vertical arrows in Fig. 8), which corresponds to the Curie temperature of ferrite and/or martensite in the as-homogenized alloys [51]. For 9Ni, 12Ni, and 15Ni alloys, an exothermic reaction occurred in the approximate temperature range 375–625 °C as marked by a dashed rectangle in Fig. 8.

During dilatometry heating at a significantly higher heating rate of 20 K/s compared to the DSC experiments, a reduction in the CTE_a occurred in the alloys that exhibited an exothermic reaction (dashed rectangle in Fig. 9). The decrease in the CTE_a indicates a reaction associated with a net contraction [52]. The proximity of the temperature ranges for the exothermic reaction and the CTE_a decrease indicates that they are due to a common mechanism with a temperature shift caused by the higher heating rate in dilatometry. Due to the presence of high martensite fractions in 9Ni, 12Ni, and 15Ni alloys, the exothermic reaction and CTE_a decrease can be attributed to the aging of martensite and are the first indications for the occurrence of B2-(Ni,Fe)Al in the martensite phase of these steels. The formation of B2 phase is also predicted by the thermodynamic equilibrium calculation results in Fig. 7.

The large CTE_a drops for the 9Ni, 12Ni, and 15Ni alloys at temperatures above 700 °C (Fig. 9) are due to the martensite-to-austenite reversion in these alloys. The clear CTE_a increase observed for the 6Ni alloy at temperatures above approximately 700 °C is thought to be due to the dissolution of pre-existing precipitates. This is based on the dilatometry analyses of ferritic alloys containing B2-(Ni,Fe)Al precipitates, where the Ni and Al enrichment of ferrite upon B2 dissolution has been found to expand the ferrite lattice and increase the CTE_a [31,53]. On this basis, B2 precipitates are expected to have formed in ferrite phase of the 6Ni alloy during cooling from the homogenization temperature. Although precipitate dissolution reactions and associated increase in the CTE_a are similarly expected for 9Ni, 12Ni, and 15Ni alloys in which B2 formation occurs during dilatometry heating, the concurrent contraction due to the martensite-to-austenite reversion in

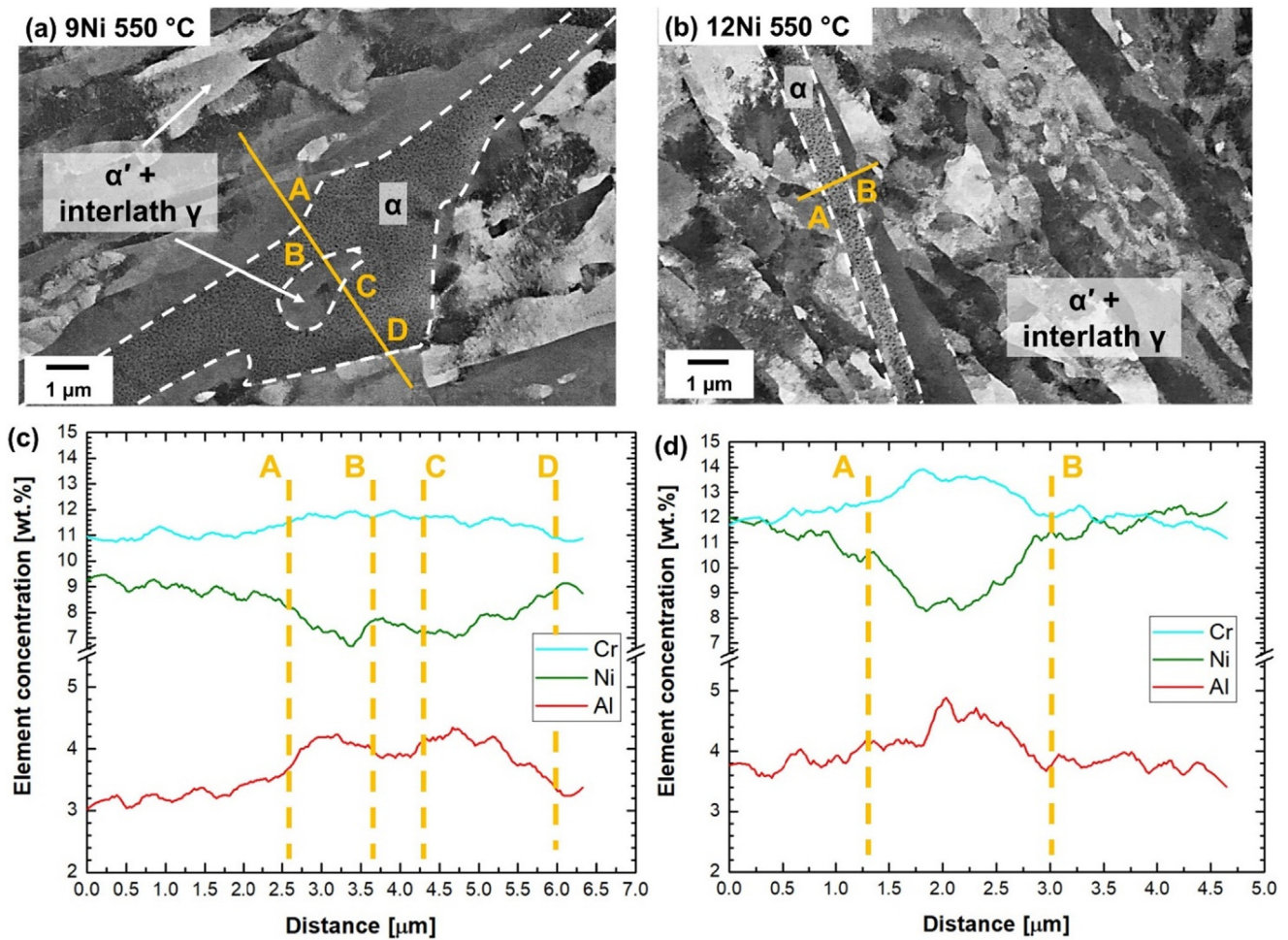


Fig. 4. SEM analysis of 9Ni (a,c) and 12Ni (b,d) alloys in aged condition: (a,b) electron channeling contrast micrographs; (c,d) EDS line scans showing the variation of alloying elements along the lines marked in (a) and (b).

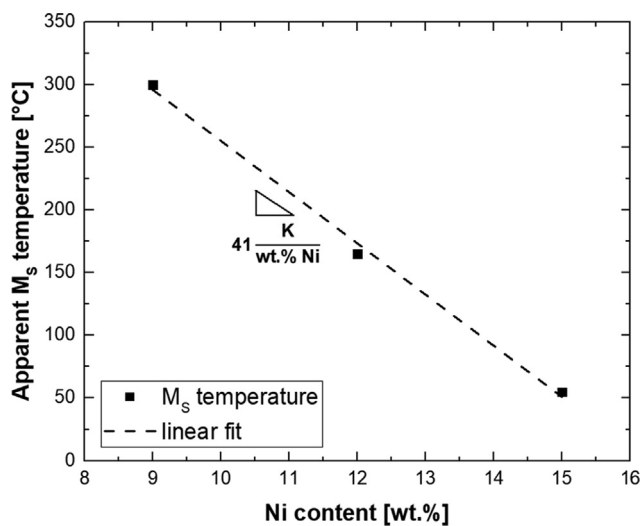


Fig. 5. Dependence of M_s temperature on Ni content.

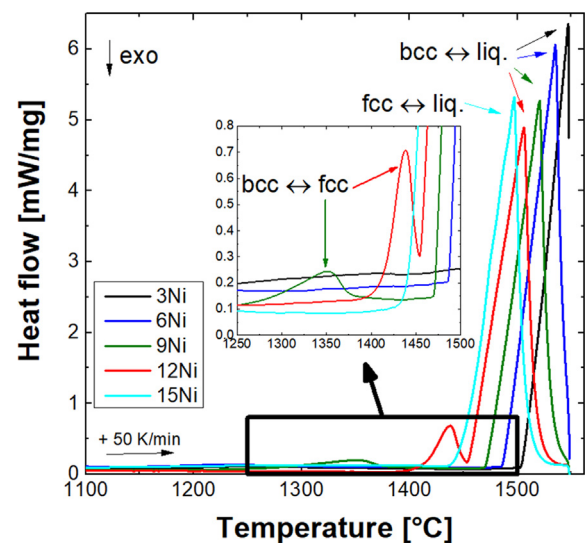


Fig. 6. DSC results during heating up to 1550 °C for the interpretation of the sequence of transformation during solidification. The inset shows a magnified view of the temperature range between 1250 and 1500 °C, over which the $\text{bcc} \leftrightarrow \text{fcc}$ phase transformation takes place for 9Ni and 12Ni alloys.

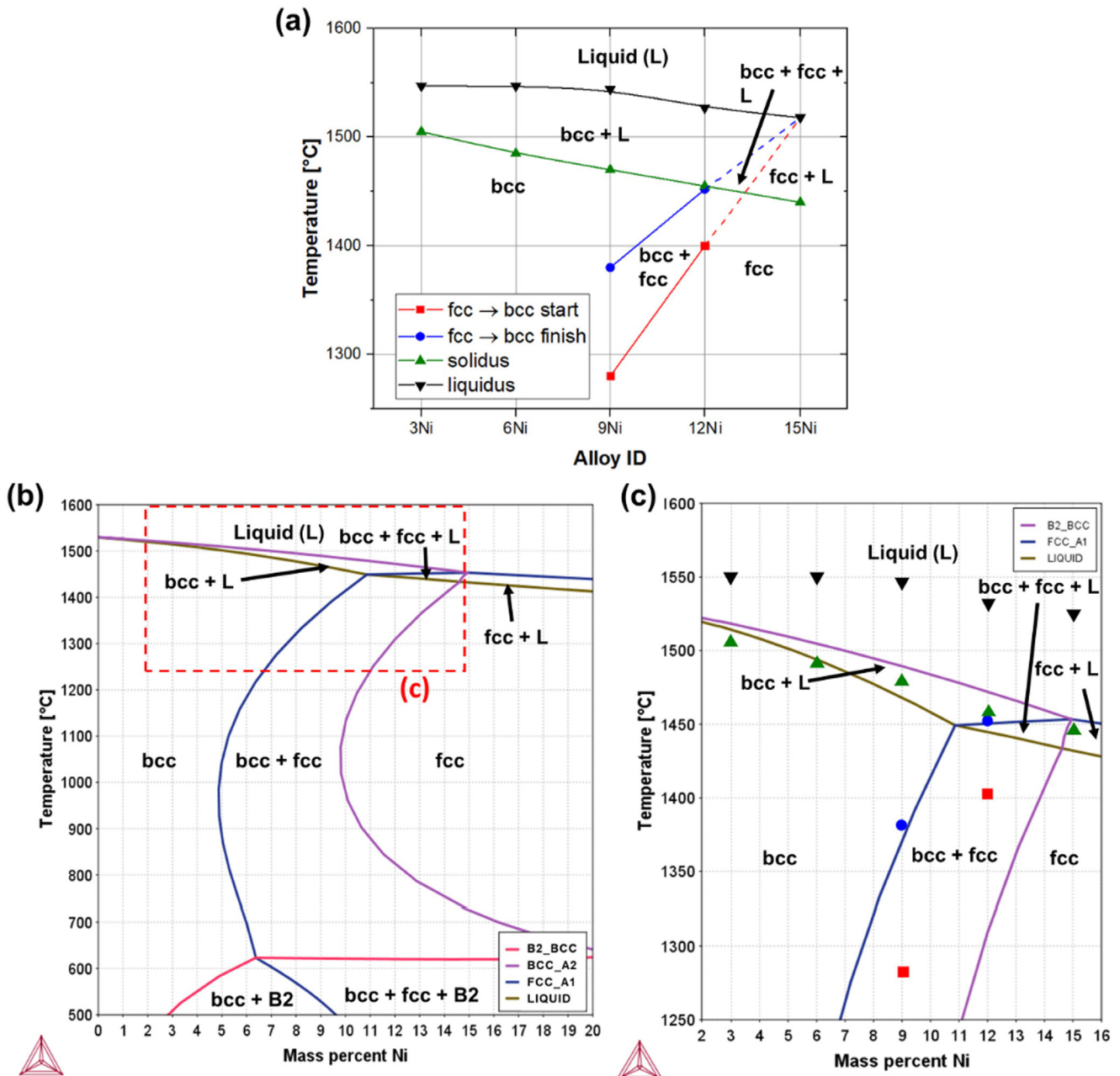


Fig. 7. Comparison of the phase transformation temperatures determined based on the DSC signal during continuous heating (a) and the results calculated by Thermo-Calc (b). (c) shows a magnified view of the area marked by a dashed rectangle in (b). For the sake of ready comparison, the DSC-based transformation temperatures marked in (a) are superimposed in (c).

these alloys has likely masked these expansions. In the DSC results of Fig. 8, the endothermic peaks immediately above the respective Curie temperatures (endothermic doublets) are expected to be due to these concurrent reactions.

3.2.2. Evolution of mechanical properties during aging

Hardness testing was done after aging for 5 min in the temperature range 300–600 °C. According to the results shown in Figs. 10, 3Ni and 6Ni alloys exhibit only a slight increase in hardness at temperatures above 350 °C. In contrast, the rest of alloys with primarily martensitic matrix microstructures experience significant age hardening at temperatures above 320 °C. For the 12Ni alloy, which exhibited the highest peak hardness of all alloys, the mean hardness increased from 381 HV5 at 320 °C to 623 HV5 at

550 °C. This can be explained by the high martensite fraction of the 12Ni alloy compared to 9Ni and 15Ni alloys, thereby its highest potential for precipitation hardening upon aging. The temperature range over which noticeable hardening occurs is consistent with the results of thermal analyses (temperature ranges marked by dashed rectangles in Figs. 8 and 9). The slight deviations can be explained by the fact that the thermal analyses were conducted during continuous heating, whereas the hardness tests were obtained after isothermal heat treatments for 5 min.

Conversion of the peak hardness to ultimate tensile strength according to the ASTM A370 standard [54] implies an estimated ultimate tensile strength of 2200 MPa (319 ksi) for the 12Ni alloy aged at 550 °C. An ultimate tensile strength in excess of 2070 MPa (300 ksi) would make the 12Ni alloy meet the strength

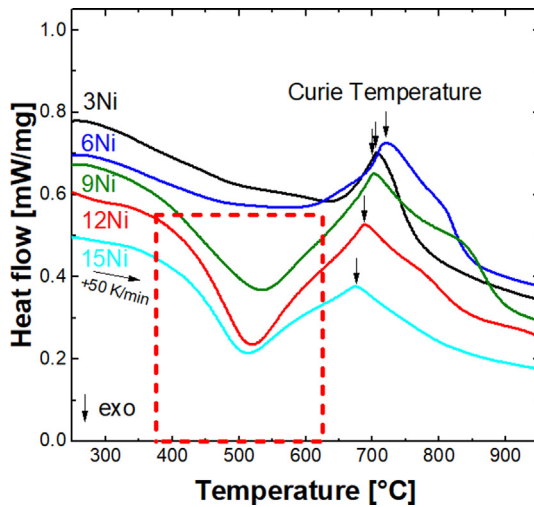


Fig. 8. DSC measurements during continuous heating. The broad exothermic peak of 9Ni, 12Ni, and 15Ni alloys between 375 °C and 625 °C is marked by a dashed rectangle. The peaks observed in the vicinity of 700 °C in all curves are due to the Curie temperature. For clarity, the curves have been translated vertically.

requirements of the 18Ni maraging steel grade 300, in which the hardening of martensite occurs via the precipitation of $\text{Ni}_3(\text{Ti},\text{Mo})$ intermetallics [55,56]. The time and temperature window for the aging of the present alloy system is also very similar to those applicable to maraging steels. Compared to maraging steels, however, the present alloy system offers the advantage of a lower density due to higher Al and lower Ni contents, enhanced corrosion and surface oxidation properties due to the presence of Cr and Al, and a lower cost due to the lower concentration of Ni and the absence of elements such as Co, Mo, and Ti. The hardness values obtained in the present case are also superior to those achieved with standard precipitation-hardenable stainless steel grades such as the 15-5PH and 17-4PH grades, in which the peak hardness after the formation of Cu precipitates in martensite barely exceeds 500 HV [57–59].

To corroborate the strength levels determined from the hardness data, microtensile specimens of 9Ni and 12Ni alloys were tested in both solution-annealed and aged conditions. Tensile

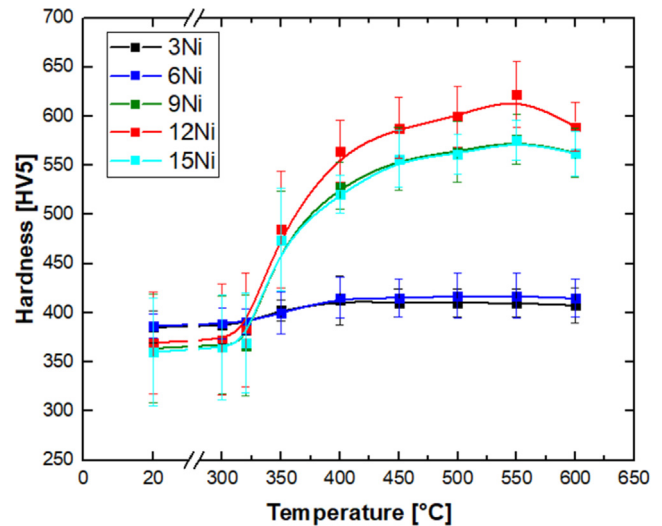


Fig. 10. Vickers hardness values after aging for 5 min.

stress–strain curves for 2 microtensile specimens in each condition are shown in Fig. 11. Stress–strain curves of both alloys in the solution-annealed condition show a more or less similar progression characterized by an early onset of necking and a few percent of post-uniform elongation. Stress–strain curves in the aged condition, on the other hand, are characterized by fracture without plastic deformation. The maximum tensile stress levels in both conditions, particularly in the aged condition, are significantly short of expectations based on the conversion of hardness data according to the ASTM A370 standard [54].

The lack of tensile ductility and ability to work harden to high strength levels in the aged 9Ni and 12Ni alloys is in contrast to the observations made for an Al-alloyed maraging steel strengthened by B2-Ni(Al,Fe) precipitates with an ordered B2 structure [60]. The favorable combination of strength and ductility in the latter work was attributed to the low lattice misfit of the coherent precipitates with the martensitic matrix. Under ideal processing conditions, precipitation-hardenable stainless steels and maraging steels exhibit fully martensitic microstructures in the solution-annealed condition. In contrast, martensite in the 9Ni and 12Ni alloys in the present work are separated by ferrite lamellae.

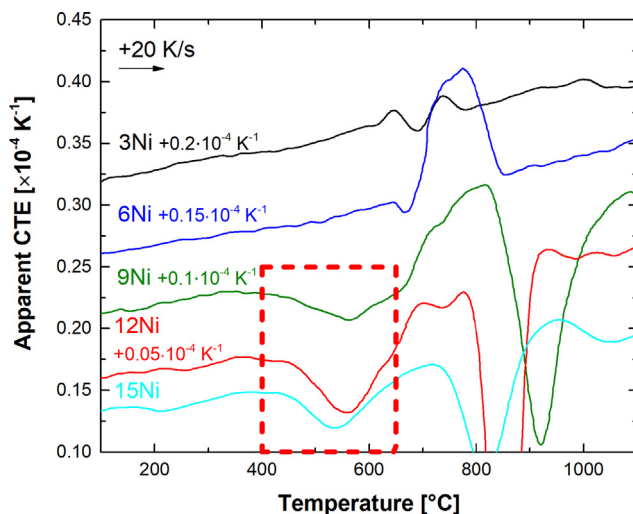


Fig. 9. Dilatometry CTE_a values during continuous heating. The CTE_a decrease for 9Ni, 12Ni, and 15Ni alloys between 400 °C and 650 °C is marked by a dashed rectangle. For clarity, curves have been translated vertically by the increments marked on each curve.

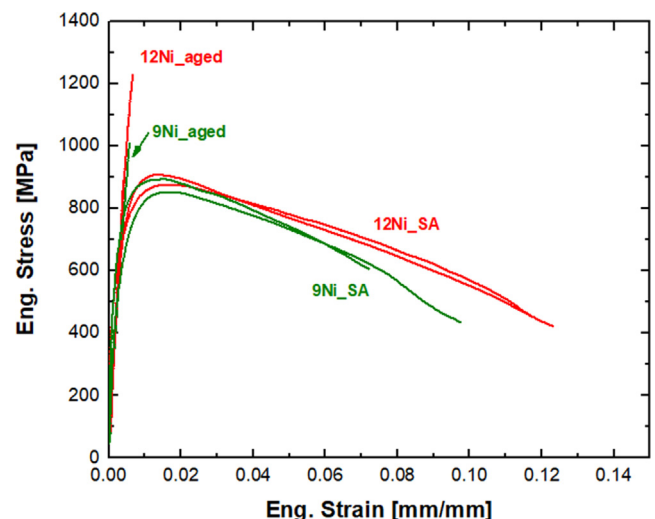


Fig. 11. Engineering stress–strain curves of 9Ni and 12Ni alloys in the solution-annealed (labeled SA) and aged conditions.

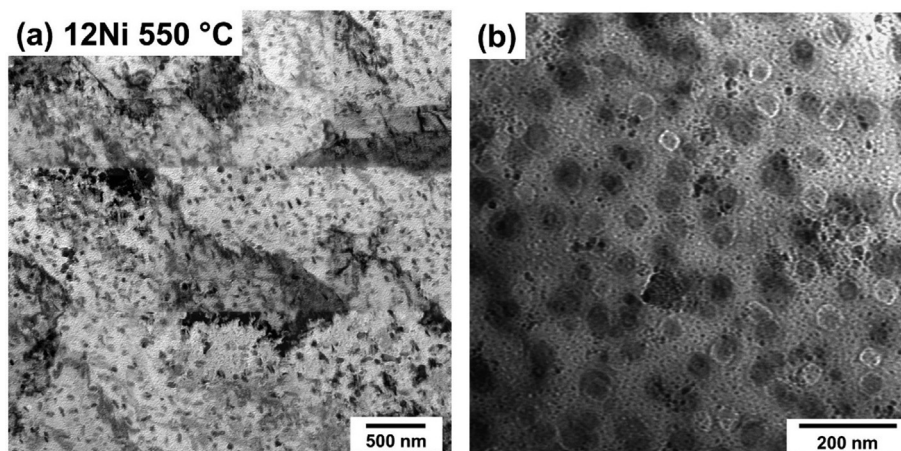


Fig. 12. TEM bright-field micrographs of ferrite in the 12Ni alloy after aging at 550 °C.

Although the ferrite lamellae present at the solution annealing temperature or formed during cooling to RT may also be strengthened by B2-(Ni,Fe)Al formation, their hardening response remains inferior to that of the martensite [61,62].

TEM micrographs in Fig. 12 exemplifies the existence of an array of precipitates, nearly 50 nm in diameter, in the ferrite phase of the aged 12Ni alloy. These precipitates are expected to have grown to this size during cooling from the solution annealing temperature. On the basis of their relatively large size, contrast due to precipitates in ferrite was also noticeable in the SEM micrographs of 9Ni and 12Ni alloys (dark spots in Fig. 4(a,b)). The presence of soft zones of ferrite is considered to be the main contributor to the early fracture of 9Ni and 12Ni alloys in the aged condition. In other words, the ability of aged microstructures to harden to tensile strength levels commensurate with the hardness values is compromised by decohesion along soft ferrite regions. The situation is aggravated by the non-optimal spatial arrangement of ferrite; due to the absence of thermomechanical processing steps such as rolling and forging operations, ferritic regions are not necessarily aligned parallel to the loading direction. This amplifies their negative impact on tensile ductility. Solution annealing conditions associated with a fully martensitic microstructure after quenching to RT are expected to alleviate embrittlement of the present alloy system.

Local strength variations originating from the non-uniform distribution of alloying elements, in particular Al and Ni which are essential to the age hardening response of the present alloy system, may also exist within the martensite phase. Additional factors with a negative influence on the tensile ductility of aged alloys are discussed in the following.

The optical micrographs shown in Fig. 3(a,d) imply a coarse prior austenite grain size for 9Ni and 12Ni alloys. Maintaining a fine prior austenite grain size in martensitic steels is an important requirement for the reliable use of martensitic steels in structural applications [63]. This is achieved by measures such as the addition of microalloying elements or by thermomechanical processing. These strategies were not used in the present work. Another possible contributor to the low ductility of the present alloys in the aged condition might have been the use of non-optimal aging conditions; aging conditions adopted in the present work were selected on the mere basis of attaining peak hardness within a short time. Peak hardness is commonly obtained by aging for a few hours, which necessitates a relatively low aging temperature [56,59,64]. Overaging and multi-step aging are among other strategies with a possible beneficial effect. Microstructure and strength variations are also thought to have facilitated early necking and

underestimated tensile strengths in the solution-annealed condition.

3.2.3. Microstructures in the aged condition

To identify the origin of the aging reactions implied by thermal analysis results and hardness measurements, TEM analyses were done for the 12Ni alloy in the peak-aged condition. Fig. 13(a,b) show bright-field and dark-field TEM micrographs of the martensite constituent. The micrographs reveal the presence of a high density of fine precipitates (~5 nm in diameter). These precipitates are almost an order of magnitude smaller than the precipitates detected in ferrite. Observation of the highest hardness in this condition implies noticeable interactions between precipitates and dislocations. This is a typical precipitate size for precipitation-hardenable steels strengthened by Cu precipitates [65] intermetallic phases [66]. Coherency strains between matrix and precipitates are expected to have a major contribution to the strength in this size range. The selected area electron diffraction (SAED) pattern in Fig. 13(c) indicates that the precipitates are ordered B2-(Ni,Fe) Al intermetallics with a CsCl-type crystal structure (Strukturbericht: B2) [25,67]. TEM-EDS results in Fig. 13(d) reveal the partitioning of elements between B2 precipitates and matrix. Obviously, precipitates are mainly enriched with Ni and Al, while Fe and Cr are rejected to the matrix. This is in good agreement with existing reports on Ni- and Al-containing martensitic [60,64,68] and ferritic [69,70] stainless steels in which intermetallic precipitates with B2 ordering are analyzed by atom probe tomography.

Due to the high volume fraction of precipitates, their crystal structure can also be studied by XRD measurements. XRD patterns of the 12Ni alloy before and after aging at 550 °C are shown in Fig. 14. In the specimen without aging, only ferrite peaks could be detected. Since B2 crystal structure is a superlattice ordered structure of ferrite, its formation would lead to diffraction peaks majority of which overlapping with those of the matrix. Nevertheless, additional peaks will also occur the most characteristic of which being (100) [2,17]. The peak occurring at $2\theta = 30.94^\circ$ is a clear indication for the presence of B2 in the aged condition.

Based on the SAED and XRD analyses of the 12Ni alloy in the aged condition, the strengthening noted in hardness and tensile tests is clearly related to the formation of a high density of B2-(Ni,Fe)Al precipitates. The age hardening response is superior to that of conventional precipitation-hardenable stainless steels such as 15-5PH and 17-4PH steels. Further enhancement of strength properties might be possible by optimizing aging conditions. The optimization must also take account of the ductility requirements. The elimination of ferrite and enabling a uniform aging response

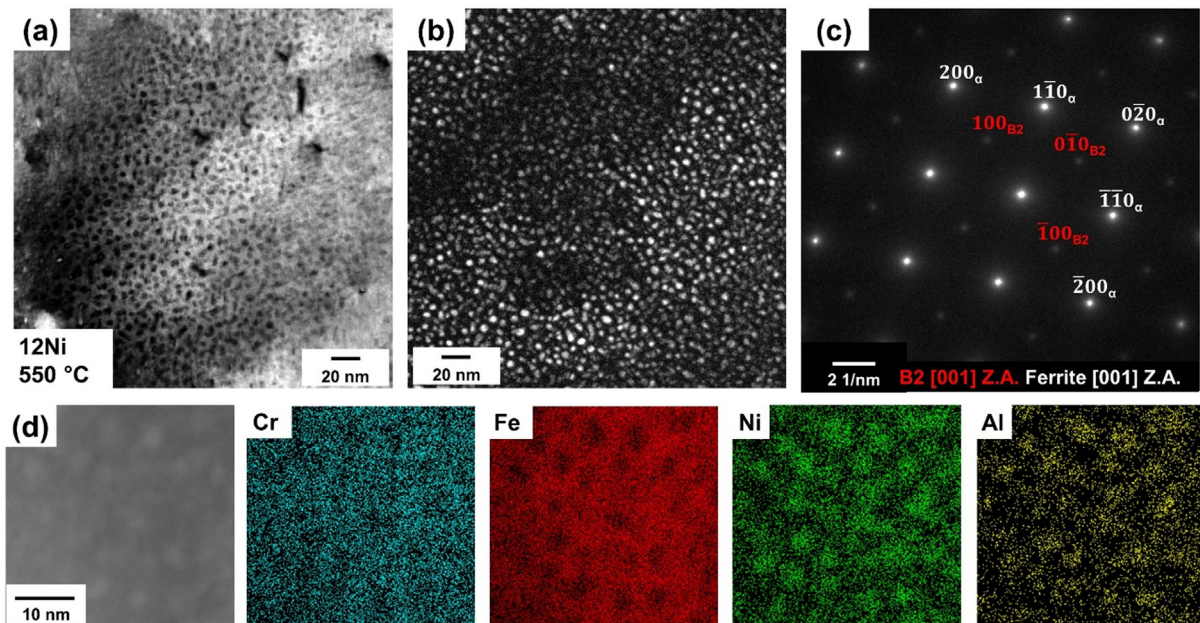


Fig. 13. TEM results for the martensite constituent in the 12Ni alloy after solution annealing and aging at 550 °C for 5 min: (a) bright-field and (b) dark-field micrographs highlighting precipitates; (c) SAED pattern recorded from the region shown in (a) and (b); (d) TEM-EDS maps showing the distribution of elements between precipitates and the martensitic matrix. e.

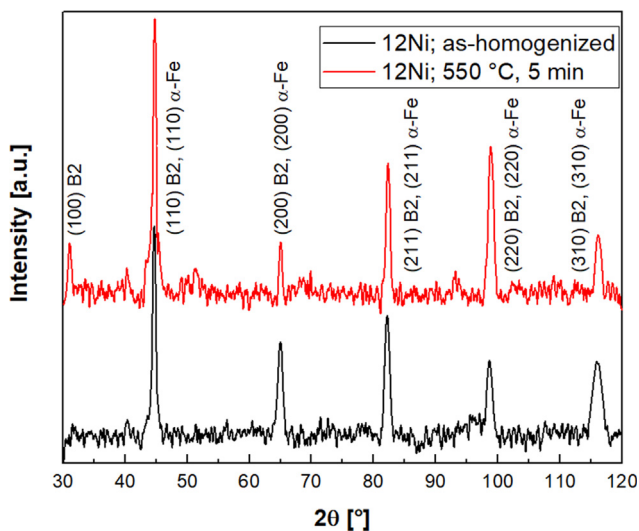


Fig. 14. XRD pattern of 12Ni alloy before and after aging at 550 °C.

throughout the material are prerequisites for a favorable balance of strength and ductility in the present alloy system.

4. Conclusions

The age hardenability of aluminum-alloyed lightweight stainless steels with the base chemical composition Fe–10.5Cr–3Al (wt.%) and Ni concentrations between 3 and 15 wt.% was studied. The following conclusions were drawn:

1. The solidification mode of the alloys was found by differential scanning calorimetry measurements to change from ferritic to austenitic as the Ni concentration increased. The experimental

results showed a reasonable agreement with the thermodynamic calculations.

2. Alloys containing 3 and 6 wt.% Ni (3Ni and 6Ni) exhibited almost fully ferritic matrix microstructures and a poor age hardening response. Alloys containing 9, 12, and 15 wt.% Ni (9Ni, 12Ni, and 15Ni), on the other hand, developed primarily martensitic microstructures at room temperature.
3. Differential scanning calorimetry measurements of the primarily martensitic 9Ni, 12Ni, and 15Ni alloys at a heating rate of 50 K/min indicated the occurrence of an exothermic reaction in the approximate temperature range 375–625 °C. Dilatometry measurements indicated that the exothermic reaction was also associated with a net contraction.
4. Hardness measurements of 9Ni, 12Ni, and 15Ni alloys after aging for 5 min indicated a significant hardening taking place already at 350 °C. For the 12Ni alloy with the highest fraction of martensite, peak hardnesses in excess of 600 HV were achieved in the aged condition. This hardness level is comparable to those obtained with the more costly, heavier, and less corrosion resistant 18Ni maraging steels and superior to those of the standard precipitation-hardenable martensitic stainless steels.
5. Tensile tests of 9Ni and 12Ni in the solution-annealed condition indicated an early onset of necking. The maximum stresses during tensile tests were lower than the ultimate tensile strength levels expected based on the conversion of hardness values. Tensile specimens aged at peak hardness failed in the elastic deformation range. Poor tensile ductilities were primarily attributed to the microstructural and chemical composition inhomogeneities originating from the solidification segregation. In the particular case of aged specimens, the presence of relatively soft ferrite zones between the hard martensitic regions was responsible for the early fracture.
6. Transmission electron microscopy examinations in the aged condition revealed that the age hardening was due to the formation of (Ni,Fe)Al precipitates with B2 crystal structure.

5. Data availability

The raw/processed data required to reproduce these findings cannot be shared at this time as the data also forms part of an ongoing study.

Declaration of Competing Interest

The authors declare that they have no known competing financial interests or personal relationships that could have appeared to influence the work reported in this paper.

Acknowledgement

The authors thank the German Research Foundation (Deutsche Forschungsgemeinschaft) for the financial support of this work under Grant No. MO 2580/2-2 (274385700).

References

- [1] Bhadeshia H, Honeycombe R. *Steels: Microstructure and Properties*. s.l.: Butterworth-Heinemann; 2017.
- [2] S.-H. Kim, H. Kim, N.J. Kim, Brittle intermetallic compound makes ultrastrong low-density steel with large ductility, *Nature* 518 (7537) (2015) 77–79, <https://doi.org/10.1038/nature14144>.
- [3] J. Herrmann, G. Inden, G. Sauthoff, Deformation behaviour of iron-rich iron-aluminum alloys at low temperatures, *Acta Materialia* 51 (10) (2003) 2847–2857, [https://doi.org/10.1016/S1359-6454\(03\)00089-2](https://doi.org/10.1016/S1359-6454(03)00089-2).
- [4] H. Kim, D.-W. Suh, N.J. Kim, Fe-Al-Mn-C lightweight structural alloys: a review on the microstructures and mechanical properties, *Sci Technol Adv Mater* 14 (1) (2013) 14205, <https://doi.org/10.1088/1468-6996/14/1/014205>.
- [5] J.R. Davis (Ed.), *Stainless steels*, 2nd ed., Materials Park, Ohio, ASM International, 1996.
- [6] M. Wendler, M. Hauser, O. Fabrichnaya, L. Krüger, A. Weiß, J. Mola, Thermal and deformation-induced phase transformation behavior of Fe-15Cr-3Mn-3Ni-0.1N-(0.05–0.25)C austenitic and austenitic-martensitic cast stainless steels, *Materials Science and Engineering: A* (2015;645:28–39), <https://doi.org/10.1016/j.msea.2015.07.084>.
- [7] Wendler M, Mola J, Krüger L, Weiß A. Experimental Quantification of the Austenite-Stabilizing Effect of Mn in CrMnNi As-Cast Stainless Steels. *steel research int.* 2014;85(5):803–10. <https://doi.org/10.1002/srin.201300271>.
- [8] N. Suutala, Effect of solidification conditions on the solidification mode in austenitic stainless steels, *MTA* 14 (1) (1983) 191–197, <https://doi.org/10.1007/BF02651615>.
- [9] P. Guiraldenq, Duparc O. Hardouin, The genesis of the Schaeffler diagram in the history of stainless steel, *Metall. Res. Technol.* 114 (6) (2017) 613, <https://doi.org/10.1051/metal/2017059>.
- [10] S.-J. Kim, T.-H. Lee, C.-S. Oh, Effect of Nitrogen on the Deformation Behaviour of High-Nitrogen Austenitic Stainless Steels, *steel research int.* 80 (2010) 462–472.
- [11] Mola J, Ullrich C, Kuang B, Rahimi R, Huang Q, Rafaja D et al. Austenitic Nickel- and Manganese-Free Fe-15Cr-1Mo-0.4N-0.3C Steel: Tensile Behavior and Deformation-Induced Processes between 298 K and 503 K (25 °C and 230 °C). *Metall and Mat Trans A* 2017;48(3):1033–52. <https://doi.org/10.1007/s11661-017-3960-x>.
- [12] H. Berns, V. Gavriljuk, B. Shanina, Intensive Interstitial Strengthening of Stainless Steels, *Adv. Eng. Mater.* 10 (12) (2008) 1083–1093, <https://doi.org/10.1002/adem.200800214>.
- [13] Berns H, Gavriljuk V, Riedner S. *High Interstitial Stainless Austenitic Steels*. Berlin, Heidelberg: Springer; 2013.
- [14] H. Berns, S.N. Bugajchuk, V.A. Duz, R. Ehrhardt, V.G. Gavriljuk, Y.N. Petrov, et al., Phase transformations during tempering of the Fe-15Cr-1Mo martensites containing nitrogen or carbon, *Steel Research* 65 (10) (1994) 444–450, <https://doi.org/10.1002/srin.199401191>.
- [15] M. Wendler, B. Reichel, R. Eckner, O. Fabrichnaya, L. Krüger, A. Weiß, et al., Effect of Vanadium Nitride Precipitation on Martensitic Transformation and Mechanical Properties of CrMnNi Cast Austenitic Steels, *Metall and Mat Trans A* 47 (1) (2016) 139–151, <https://doi.org/10.1007/s11661-014-2716-0>.
- [16] H. Yan, H. Bi, X. Li, Z. Xu, Precipitation and mechanical properties of Nb-modified ferritic stainless steel during isothermal aging, *Materials Characterization* 60 (3) (2009) 204–209, <https://doi.org/10.1016/j.matchar.2008.09.001>.
- [17] Z. Sun, C.H. Liebscher, S. Huang, Z. Teng, G. Song, G. Wang, et al., New design aspects of creep-resistant NiAl-strengthened ferritic alloys, *Scripta Materialia* 68 (6) (2013) 384–388, <https://doi.org/10.1016/j.scriptamat.2012.10.040>.
- [18] S.M. Hao, T. Takayama, K. Ishida, T. Nishizawa, Miscibility gap in Fe-Ni-Al and Fe-Ni-Al-Co systems, *MTA* 15 (10) (1984) 1819–1828, <https://doi.org/10.1007/BF02664895>.
- [19] C. Stallybrass, A. Schneider, G. Sauthoff, The strengthening effect of (Ni, Fe)Al precipitates on the mechanical properties at high temperatures of ferritic Fe-Al-Ni-Cr alloys, *Intermetallics* 13 (12) (2005) 1263–1268, <https://doi.org/10.1016/j.intermet.2004.07.048>.
- [20] H. Ohtani, Y. Chen, M. Hasebe, Phase Separation of the B2 Structure Accompanied by an Ordering in Co-Al and Ni-Al Binary Systems, *Mater. Trans.* 45 (5) (2004) 1489–1498, <https://doi.org/10.2320/matertrans.45.1489>.
- [21] R. Taillard, A. Pineau, Room temperature tensile properties of Fe-19wt.%Cr alloys precipitation hardened by the intermetallic compound NiAl, *Materials Science and Engineering* 56 (3) (1982) 219–231, [https://doi.org/10.1016/0025-5416\(82\)90097-0](https://doi.org/10.1016/0025-5416(82)90097-0).
- [22] P.H. Kitabjian, W.D. Nix, Atomic size effects in Ni-Al based solid solutions, *Acta Materialia* 46 (2) (1998) 701–710, [https://doi.org/10.1016/S1359-6454\(97\)00249-8](https://doi.org/10.1016/S1359-6454(97)00249-8).
- [23] P.G. Self, H. Bhadeshia, W.M. Stobbs, Lattice spacings from lattice fringes, *Ultramicroscopy* 6 (1) (1981) 29–40, [https://doi.org/10.1016/S0304-3991\(81\)80175-1](https://doi.org/10.1016/S0304-3991(81)80175-1).
- [24] M. Larsen, A. Misra, S. Hartfield-Wunsch, R. Noebe, R. Gibala, Ductility Enhancement from Interface Dislocation Sources in a Directionally Solidified β ($\gamma + \gamma'$) Ni-Fe-Al Composite Alloy, *MRS Proc.* 194 (1990) 473, <https://doi.org/10.1557/PROC-194-191>.
- [25] Z.K. Teng, F. Zhang, M.K. Miller, C.T. Liu, S. Huang, Y.T. Chou, et al., New NiAl-strengthened ferritic steels with balanced creep resistance and ductility designed by coupling thermodynamic calculations with focused experiments, *Intermetallics* 29 (2012) 110–115, <https://doi.org/10.1016/j.intermet.2012.05.007>.
- [26] El-Fallah G, Ooi SW, Bhadeshia H. Effect of nickel aluminide on the bainite transformation in a Fe-0.45C-13Ni-3Al-4Co steel, and associated properties. *Materials Science and Engineering: A* 2019;767:138362. <https://doi.org/10.1016/j.msea.2019.138362>.
- [27] E. Povoden-Karadeniz, E. Kozeschnik, Simulation of Precipitation Kinetics and Precipitation Strengthening of B2-precipitates in Martensitic PH 13-8 Mo Steel, *ISIJ Int.* 52 (4) (2012) 610–615, <https://doi.org/10.2355/isijinternational.52.610>.
- [28] R. Rahimi, C. Ullrich, V. Klemm, D. Rafaja, B.C. de Cooman, H. Biermann, et al., Influence of Al on the temperature dependence of strain hardening behavior and glide planarity in Fe-Cr-Ni-Mn-C austenitic stainless steels, *Materials Science and Engineering: A* 649 (2016) 301–312, <https://doi.org/10.1016/j.msea.2015.10.005>.
- [29] R. Rahimi, C. Ullrich, D. Rafaja, H. Biermann, J. Mola, Microstructural Evolution of an Al-Alloyed Duplex Stainless Steel During Tensile Deformation Between 77 K and 473 K (–196 °C and 200 °C), *Metall and Mat Trans A* 47 (6) (2016) 2705–2716, <https://doi.org/10.1007/s11661-016-3438-2>.
- [30] N.Q. Vo, C.H. Liebscher, M.J. Rawlings, M. Asta, D.C. Dunand, Creep properties and microstructure of a precipitation-strengthened ferritic Fe-Al-Ni-Cr alloy, *Acta Materialia* 71 (2014) 89–99, <https://doi.org/10.1016/j.actamat.2014.02.020>.
- [31] R. Rahimi, P. Pekker, H. Biermann, O. Volkova, B.C. de Cooman, J. Mola, Volumetric changes associated with B2-(Ni, Fe)Al dissolution in an Al-alloyed ferritic steel, *Materials & Design* 111 (2016) 640–645, <https://doi.org/10.1016/j.matdes.2016.09.033>.
- [32] DIN EN ISO 6507-1:2018-07, *Metallische Werkstoffe - Härteprüfung nach Vickers - Teil 1: Prüfverfahren* (ISO 6507-1:2018); Deutsche Fassung EN ISO 6507-1:2018. Berlin: Beuth Verlag GmbH. <https://doi.org/10.31030/2778746>.
- [33] Duffy M, Nimer S, Zupan M, Storck S. Elucidating the Impact of Processing Parameters of Additive Manufactured Materials Using Microscale Tensile Samples. In: Shamsaei N, Daniewicz S, Hrabec N, Beretta S, Waller J, Seif M, editors. *Structural Integrity of Additive Manufactured Parts*. 100 Barr Harbor Drive, PO Box C700, West Conshohocken, PA 19428-2959: ASTM International; 2020, p. 313–333.
- [34] S. Nimer, R.K. Everett, M. Zupan, Microtensile characterization of titanium 5111 alloy mechanical properties and comparison of failure mechanisms at two microstructural length scales, *Materials & Design* 183 (2019), <https://doi.org/10.1016/j.matdes.2019.108081>.
- [35] S. Nimer, J. Wolk, M. Zupan, Local property characterization of friction stir welded Ti-5111: Transverse orientation measurements, *Acta Materialia* 61 (8) (2013) 3050–3059, <https://doi.org/10.1016/j.actamat.2013.01.065>.
- [36] M. Zupan, M.J. Hayden, C.J. Boehlert, K.J. Hemker, Development of high-temperature microsample testing, *Experimental Mechanics* 41 (3) (2001) 242–247, <https://doi.org/10.1007/BF02323140>.
- [37] R.K. Everett, M.E. Duffy, S.M. Storck, M. Zupan, A Variogram Analysis of Build Height Effects in an Additively Manufactured AISI10Mg Part, *Additive Manufacturing* 35 (2020), <https://doi.org/10.1016/j.addma.2020.101306>.
- [38] S. Nimer, J. Wolk, M. Zupan, Location and Orientation Specific Material Property Evaluation of Friction Stir Welded Ti-5111: A Microsample Approach, *Adv. Eng. Mater.* 16 (4) (2014) 452–458, <https://doi.org/10.1002/adem.201300427>.
- [39] G. Chen, R. Rahimi, G. Xu, H. Biermann, J. Mola, Impact of Al addition on deformation behavior of Fe-Cr-Ni-Mn-C austenitic stainless steel, *Materials Science and Engineering: A* 797 (2020), <https://doi.org/10.1016/j.msea.2020.140084>.
- [40] N. Suutala, Effect of manganese and nitrogen on the solidification mode in austenitic stainless steel welds, *MTA* 13 (12) (1982) 2121–2130, <https://doi.org/10.1007/BF02648382>.
- [41] B.L. Ennis, E. Jimenez-Melero, R. Mostert, B. Santillana, P.D. Lee, The role of aluminium in chemical and phase segregation in a TRIP-assisted dual phase

- steel, *Acta Materialia* 115 (2016) 132–142, <https://doi.org/10.1016/j.actamat.2016.05.046>.
- [42] W.W. Sun, Y.X. Wu, S.C. Yang, C.R. Hutchinson, Advanced high strength steel (AHSS) development through chemical patterning of austenite, *Scripta Materialia* 146 (2018) 60–63, <https://doi.org/10.1016/j.scriptamat.2017.11.007>.
- [43] Y. Hao, J. Li, X. Li, W. Liu, G. Cao, C. Li, et al., Influences of cooling rates on solidification and segregation characteristics of Fe–Cr–Ni–Mo–N super austenitic stainless steel, *Journal of Materials Processing Technology* 275 (2020), <https://doi.org/10.1016/j.jmatprotec.2019.116326> 116326.
- [44] J. Yoo, B. Kim, Y. Park, C. Lee, Microstructural evolution and solidification cracking susceptibility of Fe–18Mn–0.6C–xAl steel welds, *J Mater Sci* 50 (1) (2015) 279–286, <https://doi.org/10.1007/s10853-014-8586-4>.
- [45] C.Y. Kung, J.J. Rayment, An examination of the validity of existing empirical formulae for the calculation of ms temperature, *MTA* 13 (2) (1982) 328–331, <https://doi.org/10.1007/BF02643327>.
- [46] T. Sourmail, C. Garcia-Mateo, Critical assessment of models for predicting the Ms temperature of steels, *Computational Materials Science* 34 (4) (2005) 323–334, <https://doi.org/10.1016/j.commatsci.2005.01.002>.
- [47] K.W. Andrews, Empirical formulae for the calculation of some transformation temperatures, *J. Iron Steel Inst.* (1965) 721–727.
- [48] R. Rahimi, O. Volkova, H. Biermann, J. Mola, Thermal Analysis of the Formation and Dissolution of Cr-Rich Carbides in Al-Alloyed Stainless Steels, *Adv. Eng. Mater.* 21 (5) (2019) 1800658, <https://doi.org/10.1002/adem.201800658>.
- [49] Callister WD, Rethwisch DG. *Materials science and engineering: An introduction*. 10th ed. Hoboken, NJ: John Wiley & Sons, Inc; 2018.
- [50] Gottstein G. *Physical foundations of materials science*. Berlin: Springer; 2004.
- [51] Pepperhoff W, Acet M. *Constitution and Magnetism of Iron and its Alloys*. Berlin, Heidelberg: Springer; 2001.
- [52] J. Mola, G. Luan, Q. Huang, C. Schimpf, D. Rafaja, Cementite evolution in medium manganese twinning-induced plasticity steels, *Materialia* 2 (2018) 138–147, <https://doi.org/10.1016/j.mtl.2018.07.013>.
- [53] R. Taillard, A. Pineau, B.J. Thomas, The precipitation of the intermetallic compound NiAl in Fe–19wt.%Cr alloys, *Materials Science and Engineering* 54 (2) (1982) 209–219, [https://doi.org/10.1016/0025-5416\(82\)90115-X](https://doi.org/10.1016/0025-5416(82)90115-X).
- [54] ASTM A370–20, Standard Test Methods and Definitions for Mechanical Testing of Steel Products. West Conshohocken, PA: ASTM International. <https://doi.org/10.1520/A0370-20>.
- [55] J.M. Pardo, S.S.M. Tavares, M.P. Cindra Fonseca, M.R. Da Silva, J.M. Neto, H.F.G. Abreu, Influence of temperature and aging time on hardness and magnetic properties of the maraging steel grade 300, *J Mater Sci* 42 (7) (2007) 2276–2281, <https://doi.org/10.1007/s10853-006-1317-8>.
- [56] C. Tan, K. Zhou, W. Ma, P. Zhang, M. Liu, T. Kuang, Microstructural evolution, nanoprecipitation behavior and mechanical properties of selective laser melted high-performance grade 300 maraging steel, *Materials & Design* 134 (2017) 23–34, <https://doi.org/10.1016/j.matdes.2017.08.026>.
- [57] H.R. Habibi Bajguirani, The effect of ageing upon the microstructure and mechanical properties of type 15–5 PH stainless steel, *Materials Science and Engineering: A* 338 (1–2) (2002) 142–159, [https://doi.org/10.1016/S0921-5093\(02\)00062-X](https://doi.org/10.1016/S0921-5093(02)00062-X).
- [58] C.N. Hsiao, C.S. Chiou, J.R. Yang, Aging reactions in a 17–4 PH stainless steel, *Materials Chemistry and Physics* 74 (2) (2002) 134–142, [https://doi.org/10.1016/S0254-0584\(01\)00460-6](https://doi.org/10.1016/S0254-0584(01)00460-6).
- [59] Govindaraj V, Hodgson P, P Singh R, Beladi H. Precipitation reactions in 12Cr–3Ni–3Mn–3Cu–0.15Nb steel. *Materials Science and Engineering: A* 2021;808:140909. <https://doi.org/10.1016/j.msea.2021.140909>.
- [60] S. Jiang, H. Wang, Y. Wu, X. Liu, H. Chen, M. Yao, et al., Ultrastrong steel via minimal lattice misfit and high-density nanoprecipitation, *Nature* 544 (7651) (2017) 460–464, <https://doi.org/10.1038/nature22032>.
- [61] R. Rahimi, B.C. de Cooman, H. Biermann, J. Mola, Microstructure and mechanical properties of Al-alloyed Fe–Cr–Ni–Mn–C stainless steels, *Materials Science and Engineering: A* 618 (2014) 46–55, <https://doi.org/10.1016/j.msea.2014.09.001>.
- [62] Z.K. Teng, C.T. Liu, G. Ghosh, P.K. Liaw, M.E. Fine, Effects of Al on the microstructure and ductility of NiAl-strengthened ferritic steels at room temperature, *Intermetallics* 18 (8) (2010) 1437–1443, <https://doi.org/10.1016/j.intermet.2010.03.026>.
- [63] E.J. Seo, J.G. Speer, D.K. Matlock, R.L. Cryderman, Effect of Mo in Combination with Nb on Austenite Grain Size Control in Vacuum Carburizing Steels, *J. of Mater Eng and Perform* 29 (6) (2020) 3575–3584, <https://doi.org/10.1007/s11665-020-04751-8>.
- [64] Y. Li, W. Yan, J.D. Cotton, G.J. Ryan, Y. Shen, W. Wang, et al., A new 1.9GPa maraging stainless steel strengthened by multiple precipitating species, *Materials & Design* (2015;82:56–63.), <https://doi.org/10.1016/j.matdes.2015.05.042>.
- [65] T. Zhou, R. Prasath Babu, J. Odqvist, H. Yu, P. Hedström, Quantitative electron microscopy and physically based modelling of Cu precipitation in precipitation-hardening martensitic stainless steel 15–5 PH, *Materials & Design* 143 (2018) 141–149, <https://doi.org/10.1016/j.matdes.2018.01.049>.
- [66] L. Sun, T.H. Simm, T.L. Martin, S. McAdam, D.R. Galvin, K.M. Perkins, et al., A novel ultra-high strength maraging steel with balanced ductility and creep resistance achieved by nanoscale β -NiAl and Laves phase precipitates, *Acta Materialia* 149 (2018) 285–301, <https://doi.org/10.1016/j.actamat.2018.02.044>.
- [67] Dorantes-Rosales HJ, Lopez-Hirata VM, Gonzalez-Velazquez JL, Cayetano-Castro N, Saucedo-Muñoz ML. Precipitation Process in Fe–Ni–Al-based Alloys. In: Aliofkhaezrai M, editor. *Superalloys*. InTech; 2015.
- [68] Z. Guo, W. Sha, D. Vaumousse, Microstructural evolution in a PH13–8 stainless steel after ageing, *Acta Materialia* 51 (1) (2003) 101–116, [https://doi.org/10.1016/S1359-6454\(02\)00353-1](https://doi.org/10.1016/S1359-6454(02)00353-1).
- [69] Z.K. Teng, M.K. Miller, G. Ghosh, C.T. Liu, S. Huang, K.F. Russell, et al., Characterization of nanoscale NiAl-type precipitates in a ferritic steel by electron microscopy and atom probe tomography, *Scripta Materialia* 63 (1) (2010) 61–64, <https://doi.org/10.1016/j.scriptamat.2010.03.013>.
- [70] S. Huang, G. Ghosh, X. Li, J. Ilavsky, Z. Teng, P.K. Liaw, Effect of Al on the NiAl-Type B2 Precipitates in Ferritic Superalloys, *Metall and Mat Trans A* 43 (10) (2012) 3423–3427, <https://doi.org/10.1007/s11661-012-1318-y>.